

## **RF-INTERROGATED END-STATE CHIP-SCALE ATOMIC CLOCK**

**A. M. Braun**

**Sarnoff Corporation**

**201 Washington Road, Princeton, NJ 08543, USA**

**Phone: (609) 734 3143, FAX: (609) 734 2565**

**E-mail: [abraun@sarnoff.com](mailto:abraun@sarnoff.com)**

**T. J. Davis, M. H. Kwakernaak, J. J. Michalchuk,**

**A. Ulmer, W. K. Chan, J. H. Abeles, Z. A. Shellenbarger**

**Sarnoff Corporation**

**201 Washington Road, Princeton, NJ 08543, USA**

**Y-Y. Jau and W. Happer**

**Department of Physics, Princeton University**

**Princeton, NJ 08540, USA**

**T. McClelland, H. Fruehauf, R. Drap, W. Weidemann, and M. Variakojis**

**Frequency Electronics, Inc.**

**55 Charles Lindbergh Blvd., Mitchell Field NY 11553, USA**

### **Abstract**

*A chip-scale atomic clock implemented with end-state physics has been fabricated and characterized. Batch-fabricated components were specifically designed and developed to enable integration within a small form-factor package. The full physics package, implemented with CW VCSEL optical pump, direct end-state hyperfine RF and Zeeman interrogation for magnetic field stabilization, was demonstrated within a 4 cm<sup>3</sup> volume, consuming 25 mW of power, and exhibiting an Allan deviation stability of 6×10<sup>-11</sup>√τ. In addition, end-state signal contrast exceeded 40% from millimeter-scale vapor cells with buffer-gas pressures exceeding 2.5 atmospheres, demonstrating the route to submillimeter vapor-cells within high-performance CSACs for high shock/vibration environments.*

## **INTRODUCTION**

Low power consumption chip-scale atomic clocks (CSACs) will enable new applications, including navigation and secure communications within GPS-denied environments, active sensor nodes, and wide-bandwidth coherent digital signal processing. Clock techniques such as coherent population trapping on

the 0-0 hyperfine transition (CPT), optically pumped by a circularly-polarized laser, have been demonstrated to provide low power consumption atomic clocks without the need for bulky microwave cavities or lamp-based sources [1-4]. Reduction of the CSAC volume and power consumption is dominated by the ability to miniaturize the alkali-vapor (cesium or rubidium) cell dimensions while operating within a system architecture that allows such reduction without appreciable loss of signal strength. Miniaturization of the alkali-vapor cell results in the need for high background buffer-gas pressure to mitigate alkali-wall collisions, as well as increased cell temperature to maintain an optimal optical absorption path length. Both of these effects lead to a dramatic reduction in 0-0 resonance signal strength due to optical pumping out of the 0-0 population with increased buffer-gas pressure and spin-exchange-dominated linewidth broadening with increased cell temperature (increased alkali density). End-state physics can provide scaling advantages for clock miniaturization due to the natural optical pumping from a circularly polarized laser to the spin state of maximum angular momentum [5], allowing the generation of a large hyperfine resonance signal even in the presence of high buffer-gas pressure, as well as suppression of spin-exchange collisional broadening [6,7] from a high-temperature vapor cell.

In previous Proceedings, results were presented on components for end-state CSACs implemented with a Coherent Population Trapping (CPT) architecture [8]. To take full advantage of end-state pumping, we migrated to a non-CPT approach, utilizing CW VCSEL optical pump and direct RF interrogation, but still without use of a microwave cavity. A second servo control-loop was implemented on the Zeeman transition which, when operating with the hyperfine frequency loop, locks the system to a point of constant local magnetic field magnitude and clock output frequency.

The below proceeding will describe such a system, including a low power consumption physics-package based on the development of low-threshold, low-noise VCSEL pump lasers, thermally isolating batch-fabricated support structures with integrated heater and temperature sensors, temperature-invariant buffer-gas cesium cells of pressure from 0.1 atm to greater than 5 atm, and sub-RF-wavelength microwave feed lines for direct RF interrogation. Such a physics package was developed and implemented with dual feedback loops for simultaneous locking a local oscillator to the end-state hyperfine transition (clock output), as well as active control over the local magnetic field by locking to a Zeeman resonance, needed for end-state stabilization. Implemented with a 2 mm path length and a 0.7 atm buffer-gas cell, a high-performance end-state CSAC fully integrated into a 4 cm<sup>3</sup> physics package volume was demonstrated. This physics package consumes 25 mW power while exhibiting an Allan deviation stability of  $6 \times 10^{-11}/\sqrt{\tau}$  out to 200 seconds, based on end-state resonance signals exceeding a 50% contrast ratio. The drift was determined to be caused by temperature effects in the lab-scale electronics and system and not due to magnetic field changes, as verified by operating the same physics package on the field-insensitive 0-0 transition. Finally, a second physics package was developed utilizing a 2.5 atm buffer-gas cell. Such a high pressure cell, operating in the optically unresolved hyperfine splitting regime, was measured to still have an end-state hyperfine signal contrast ratio of 40%, demonstrating the route to submillimeter, high-pressure CSACs for low power consumption and high shock and vibration applications.

## END-STATE ATOMIC CLOCK

Traditionally, the two field independent sublevels of the atomic vapor with angular momentum quantum number  $m_F=0$  are used as the clock transition (Figure 1). Strong optical pumping with circularly polarized light at the D1 wavelength transfers most atoms into the end states ( $F=4$ ,  $m_F=-4$  or  $m_F=+4$  in cesium; Figure 1), increasing the end-state signal at the expense of the 0-0 population. In addition, as the end transition is a maximum angular momentum state, collisions between atoms in the end states do not result in a change of spin population concentration and, hence, suppresses spin-exchange collisional broadening, particularly relevant in miniature cells operating at elevated temperatures and high alkali-vapor densities.

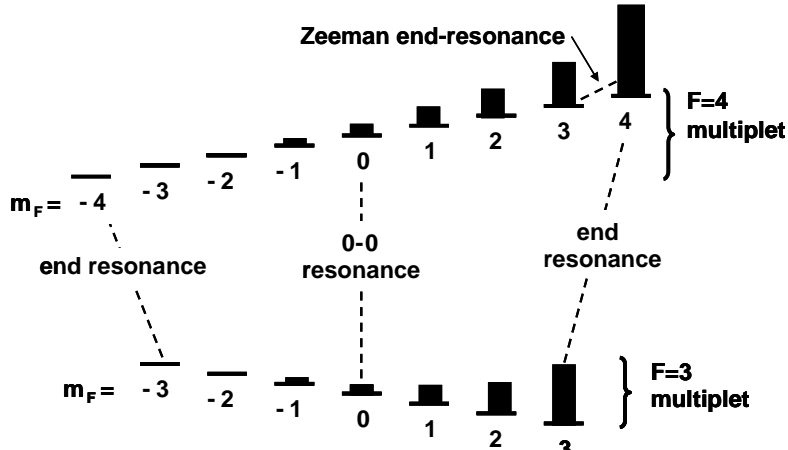


Figure 1. Schematic of ground-state hyperfine levels of  $^{133}\text{Cs}$  and populations under circularly polarized optical pumping.

A high-level description of the end-state clock configuration is shown in Figure 2. A circularly polarized CW VCSEL at the  $^{133}\text{Cs}$  D1 absorption line pumps the miniature cell. The transmission is detected with a silicon photodiode with phase-synchronous demodulation used to maintain feedback control locking. Also shown is a typical measured end-state resonance signal obtained from a 2 mm, 0.7 atm cesium vapor cell, without Zeeman interrogation.

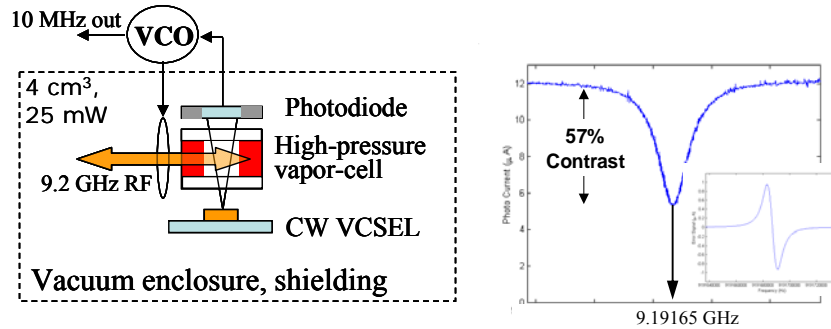


Figure 2. A RF interrogated end-state clock configuration (left) and the resulting high-contrast hyperfine resonance signal (right).

A challenge for this approach is the first-order dependence of the end-resonance frequency and, hence, clock frequency, on the magnetic field value. While the second-order dependence of the 0-0 transition clocks on magnetic field is sufficiently small and can be suppressed with adequate magnetic field shielding, end-resonance clocks require active control of the magnetic field. In general, the Zeeman splitting has a field sensitivity of  $f_{\text{Zeeman}} = \eta B$ , resulting in an end-state hyperfine frequency of  $f_{\text{End}} = f_{0-0} + 7\eta B$ , where  $\eta \sim 350 \text{ kHz/G}$ ,  $f_{0-0} = 9.19 \text{ GHz}$  for cesium, and  $B$  is the magnitude of the local magnetic field. To stabilize the clock frequency against magnetic field perturbations, the atomic-based Zeeman resonance can be interrogated and used in feedback control to stabilize the local magnetic field value. To implement such a feedback loop, we derive the Zeeman interrogation frequency from the local-oscillator clock loop and rely on the large multiplier between end-state hyperfine and Zeeman to allow the

system to quickly converge to a stable, and unique, lock point (Figure 3). In our existing CSAC, the Zeeman transition is initially set to ~30 kHz with z-axis Helmholtz coils, while the end-state hyperfine frequency is ~9.19 GHz, hence a “lever-arm” of  $10^5\text{--}10^6$ . We have demonstrated that such an approach reduces the end-state sensitivity from 2450 kHz/G to about 10 Hz/G, a mitigation in field sensitivity of over 5 orders of magnitude (Figure 4). As the Zeeman interrogation involves the same atoms that are utilized in the local-oscillator clock loop, there is an impact on overall system stability to implementing the magnetic stabilization feedback loop. As both clock and magnetic field stability loops are operated as synchronously detected feedback systems, the overall system Allan deviation becomes proportional to the strengths of both resonance signals,  $\sqrt{((1/\text{FOM}_{\text{end}})^2 + (1/\text{FOM}_Z)^2)}$ , where FOM is the resonance signal Figure-of-Merit defined as resonance contrast ratio/linewidth [9]. As both the Zeeman and the end-state hyperfine resonance signal are optimized, the impact to the system Allan deviation is about a factor of  $2\sqrt{2}$  as compared to the system stability projected from the optimized end-state hyperfine resonance alone.

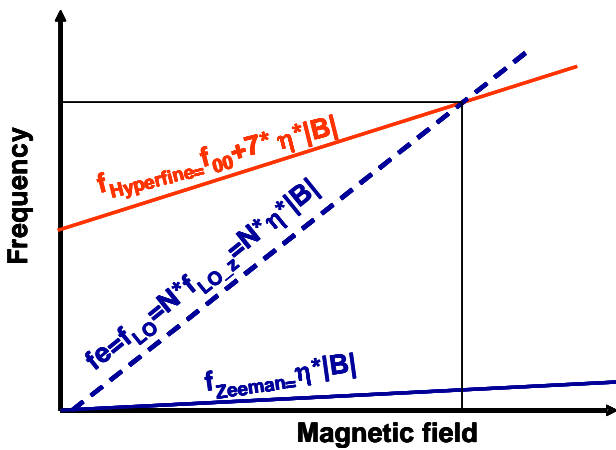


Figure 3. Graphical representation of the dual feedback loop locking to stabilize end-state resonance against magnetic field perturbations. With a large predefined integer value, the Zeeman interrogation resonance frequency can be derived from the local-oscillator frequency ( $f_{\text{Lo-Z}} = f_{\text{Lo}}/N$  with  $N\sim 10^5\text{--}10^6$ ). The bias field will adjust to bring the Zeeman resonance into lock, adjusting the end-state resonance. Due to the large integer “lever arm,” this adjustment in end-state resonance only has a small effect on the Zeeman local-oscillator frequency. In this way, both the local magnetic field and the clock end-resonance frequency quickly adjust to a stable lock point.

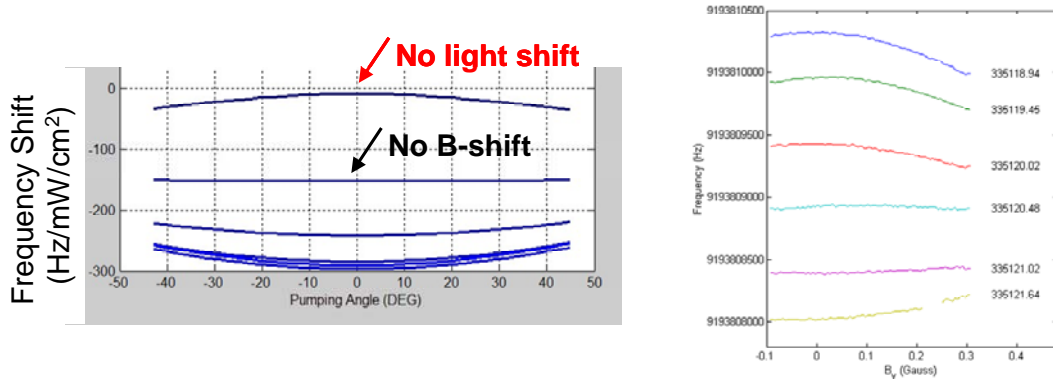


Figure 4. Left) Model; Right) Measurement of the effect of dual-locking feedback loops as a function of perturbing magnetic fields, with each curve representing a different optical frequency detuning. As seen in the model, the result of the dual feedback control is to convert the end-state magnetic field sensitivity from a linear to quadratic dependence. At one particular detuning, the system is essentially insensitive to magnetic field perturbations (left, “No B-shift”). Notably, at a slightly shifted optical detuning, the system is insensitive to an optical light shift, with a resulting quadratic dependence on magnetic field perturbations. The measurements on the right validate the model. In our fabricated CSAC, mechanical tolerancing led to a breaking of the system symmetry, yielding a slight residual linear magnetic field sensitivity of 10 Hz/G, a similar value to that experienced on the 0-0 transition, assuming a bias field of 10 mG.

The schematic of the end-state feedback-control system is shown in Figure 5. Three control loops include the servo-control on the clock frequency, magnetic field, and laser center wavelength, all driven with FM-modulated signals. The feedback loop “error signals” were obtained from the photodiode signal as a result of alkali-atom modulation of the DC VCSEL laser light. The hyperfine frequency loop was used to control the local-oscillator clock frequency; the Zeeman interrogation loop was fed back to the Z-axis Helmholtz bias coils to maintain a constant local magnetic field value; and the feedback from the cesium optical absorption profile was fed back to the VCSEL temperature control to stabilize the laser wavelength. In this way, the Zeeman resonance is used as a measure of the local magnetic field value and under feedback control, to maintain a stable clock hyperfine resonance frequency. The low-frequency FM modulation frequencies were chosen for uniqueness and ease of detection. Specific implementation utilized an x-axis coil pair to drive the Zeeman resonance at ~30 kHz with error-signal feedback to the z-axis Helmholtz bias coils. A uniform z-axis bias field is produced by a Helmholtz coil pair, as magnetic field nonuniformities will result in clock resonance line broadening due to the linear dependence on the magnetic field value.

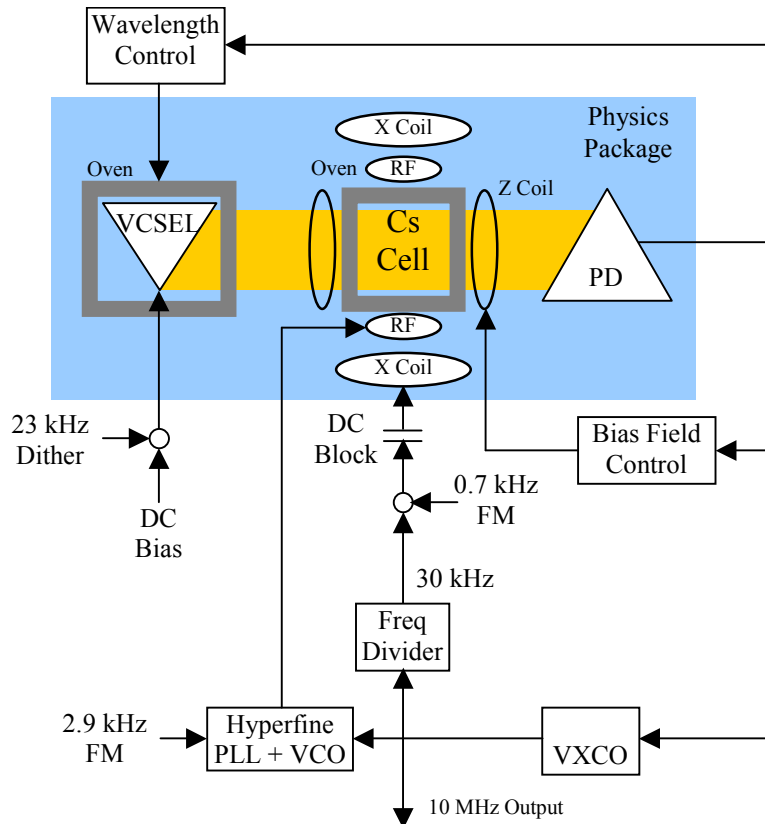


Figure 5. Detailed schematic of the end-state clock system. PI control is used to stabilize the cesium cell temperature. Feedback control was used to stabilize the VCSEL laser wavelength to the cesium optical absorption peak, clock local oscillator stabilized against the end-state hyperfine resonance and bias field magnitude stabilized against the Zeeman resonance. X-axis Zeeman interrogation results in error-signal feedback to the z-axis Helmholtz coil pair.

## BATCH-FABRICATED COMPONENTS

Batch-fabricated components were designed and developed to produce the low power consumption, compact end-state physics package, including: alkali-vapor cells, low-threshold VCSEL lasers, thermally isolating supports, and RF feed loops. The cesium-based alkali-vapor cells were fabricated from 4" silicon wafers diced into 1" square for ease of handling. An array of through-holes was etched in the high-resistance silicon prior to anodic bonding to the Pyrex base. Within an anaerobic glovebox, a controlled and repeatable cesium micro-droplet was placed in each silicon well via a pin-transfer technique. The cesium-loaded plate was then placed within an enclosure allowing for vacuum pump-down and backfilling with appropriate pressure buffer-gas mixtures. Within this environment, the top Pyrex plate was anodically bonded, creating the sealed vapor-cell cavities. In this manner, vapor cells as small as 500  $\mu\text{m}$  in dimension were fabricated with temperature-invariant ArN<sub>2</sub> buffer-gas pressures varying from 0.1 atm to greater than 5 atm. Figure 6 shows a photo of the completed cells. Note the rim of gold-colored cesium, allowing for clear aperture of optical transmission. Figure 6 also shows complete clock measurement as a function of cell temperature, showing a zero clock-frequency shift as a function

of buffer-gas temperature at an operating temperature of 118°C, as designed (a 2-mm 0.7-atm ArN<sub>2</sub> buffer gas cell).

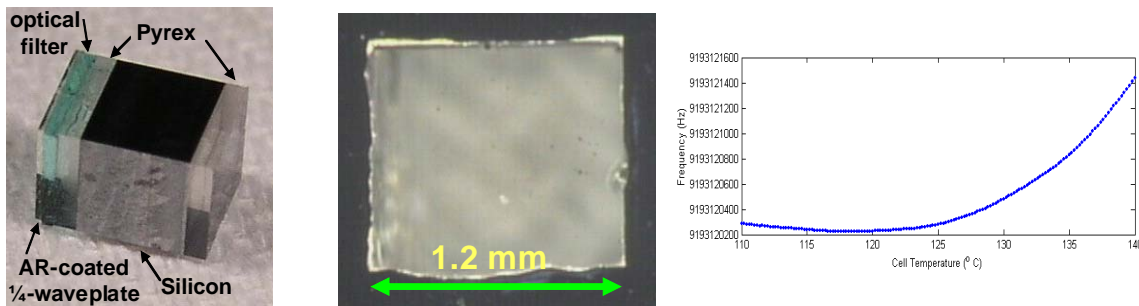


Figure 6. Anodically bonded Pyrex/silicon/Pyrex cesium vapor cell: cell with neutral density filter and anti-reflection-coated  $\frac{1}{4}$  waveplate (left); close-up of 1.2 mm cell aperture (center); cell hyperfine frequency vs. temperature plot showing the zero buffer-gas-induced temperature coefficient at 118°C (right).

The fabricated optical pump is a VCSEL laser designed for cesium D1-line pumping (894.5 nm). Low-threshold, linearly polarized, single-spatial-mode VCSELs were grown by MOCVD on 2-degree off-axis GaAs substrates. The active region of the VCSELs contains three In<sub>0.10</sub>Ga<sub>0.90</sub>As quantum wells. An Al<sub>0.98</sub>Ga<sub>0.02</sub>As layer situated above the active region was selectively oxidized to form an intracavity oxide aperture. The upper and lower mirror stacks consist of quarter-wave Al<sub>0.9</sub>Ga<sub>0.1</sub>As and Al<sub>0.06</sub>Ga<sub>0.94</sub>As pairs. The 20 top mirror layer pairs are  $\delta$ -doped and compositionally graded with a parabolic profile for low series resistance and minimal optical losses; the 30 bottom mirror layer pairs were undoped with no compositional grading for minimal optical losses. The *n*-contact was made to an intracavity A<sub>0.06</sub>Ga<sub>0.94</sub>As layer, with the pad accessible from the top of the device. Top-side bond pads were fabricated on a thick polyimide layer for low parasitic capacitance and patterned as coplanar strip lines (Figure 7). VCSEL emission was designed for a Cs D1-wavelength at an operating temperature of ~70°C. Figure 5 shows DC-biased performance with sub-300  $\mu$ A thresholds and operation at temperatures exceeding 100°C. Also shown is measured low-frequency intensity noise with a RIN value of -135 dBc/Hz at a loop bandwidth of 1kHz, enabling a RIN-limited Allan deviation of  $10^{-12}/\sqrt{\tau}$ . The side-mode suppression ratio was measured to exceed 40 dB, with device-to-device polarization measured to be linear along the GaAs crystal axis, as designed.

The wavelength nonuniformity across the wafer was typically 0.5% relative standard deviation. Importantly, the physics-package system thermal design allows for a 1.2 nm temperature tuning range due to isolated VCSEL and cesium-cell thermal zones. This allows the greater than 20% wavelength yield of the VCSELs.

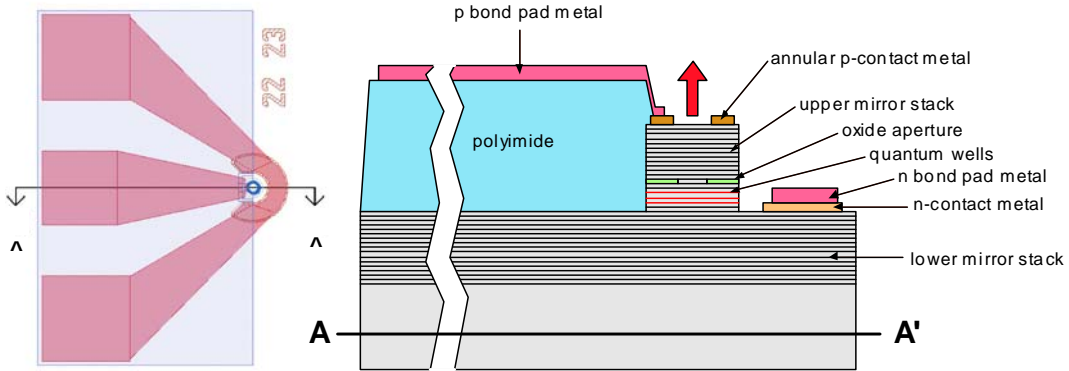


Figure 7. Schematic view of a VCSEL. A plan view is on the left and the A-A' cross-section is on the right.

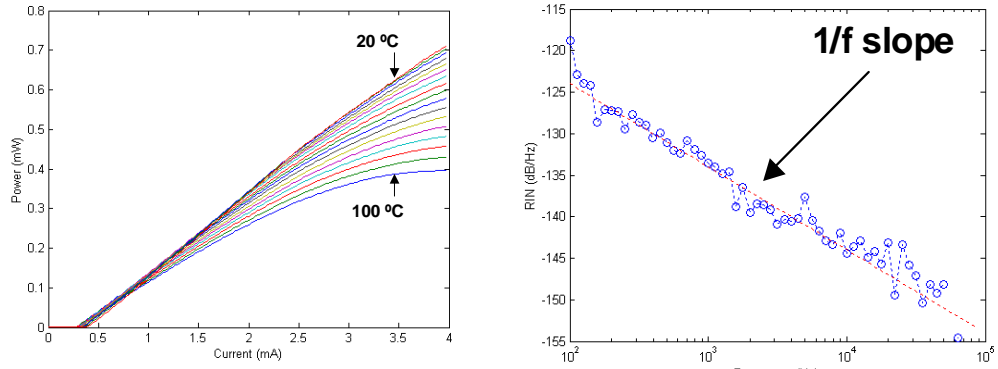


Figure 8. VCSEL power vs. current for temperatures between 20°C to 100°C in increments of 5°C (left). Measured VCSEL Relative Intensity Noise (RIN) data (right). Low noise is achieved (-135 dBc/Hz at 1 kHz frequency).

Thermally isolating structures to independently support both the VCSEL and the cesium cell were developed based on a 15  $\mu\text{m}$  thick polyimide membrane. These elements were fabricated on 4" silicon wafers with polyimide spun-on in multiple layers. Embedded within the polyimide are patterned Ti-Pt lines used as heating and temperature sensing elements. The heater and sensing traces were patterned using 10  $\mu\text{m}$  design rules. The heater and temperature sensor conductor geometry is laid out in a serpentine pattern in counter-flowing current pairs with 20 micron center-to-center spacing to cancel magnetic fields. Other processing steps include polyimide patterning, TiAu bond pad and interconnect deposition and patterning, and silicon back-side release to form 8 mm square silicon frames anchoring suspended polyimide support and thermal isolating structures (see Figure 9).

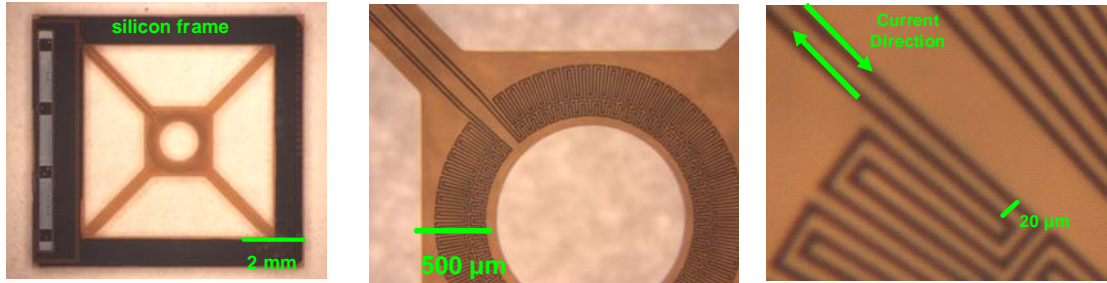


Figure 9. Micrograph of a typical flex circuit. Left: Full thermally isolating support shown fabricated on an 8 mm square silicon frame. The polyimide arms are 400  $\mu\text{m}$  wide and 15  $\mu\text{m}$  thick. Bond pads and traces are Ti-Au with a transition to Ti-Pt for thermal control at the region where the cell or VCSEL would be placed. Middle: Close-up of the vapor-cell thermal flex. The vapor cell would be bonded to two such supports, one on the input and one at the cell output. The polyimide has a hole for optical beam propagation. Right: Expanded close-up showing the 10  $\mu\text{m}$  design rule serpentine pattern used to reduce magnetic field generation from heater traces. All current-carrying traces are routed in counter-current pairs to cancel magnetic fields.

RF feed lines were developed as a lumped-element shorted stripline loop structure, whereby a 9.2 GHz oscillating current produces the needed RF magnetic field in the region of the vapor-state atoms. The input section of the RF coil board, shown in Figure 10, is a microstrip. The signal is transformed from an unbalanced to a balanced signal. The slot line carries the signal to the coils. Single-turn loops are patterned on an alumina substrate. The input microstrip is matched to the drive circuit with the balun transformer providing cancellation of stray fields and yielding the needed directionality of the B-field component of the RF field transverse through the alkali vapor cell. Note that this is designed as a nonradiating structure, with the alkali-vapor cell in the near-field of the loop magnetic-field. The system requires approximately 0.5 mA of RF current to generate the needed mG field strength, or with a 50 ohm impedance positioned with each RF line, about 12  $\mu\text{W}$  of drive power. Impedance mismatches and propagation losses in the current system increase the needed RF drive power to the -4 dBm power level.

The RF input was designed with HFSS modeling software. A model of the system used for RF simulations is shown in Figure 11. The output of the 9.19 GHz lock-in is split evenly and in-phase in the Wilkinson power splitter. A coax line carries the signal through the two-layer magnetic shield and titanium package base to the RF coil board.

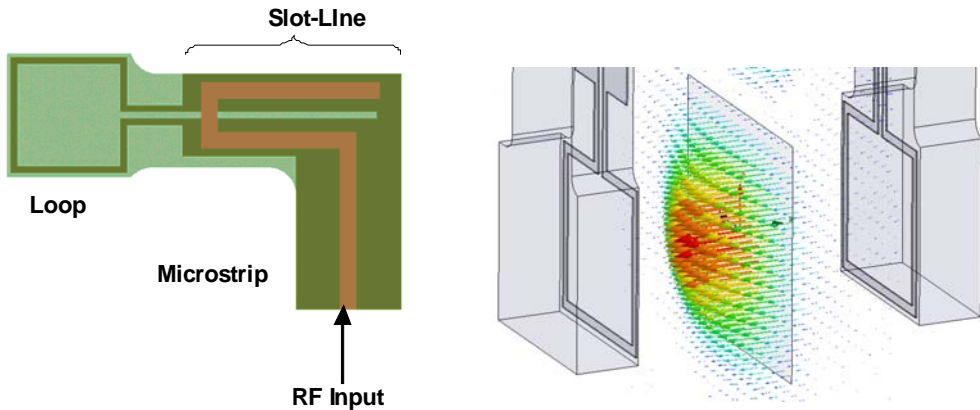


Figure 10. RF coil board layout. Left: The boards are made of two-sided 0.5 mm alumina substrate with 1 micron gold. The brown color trace is on the top side of the substrate. The dark green is on the bottom side. Note that the loop diameter is 2 mm, much smaller than the wavelength of the RF (3.2 cm in free space). Right: 9.2 GHz magnetic field plot from HFSS simulation. Driving the RF coils in phase produces field lines perpendicular to the plane of the coils. Note that this is a nonradiating structure, with the alkali atoms in the near field of the generated magnetic oscillation.

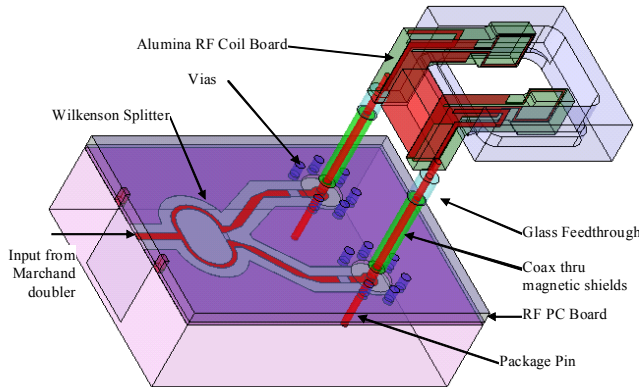


Figure 11. HFSS model of the 9.2 GHz hyperfine interrogation circuit. This model includes the final output section of the RF PC board, the transition to the feed-through pins into the vacuum package, the balun transformers, and the single loop coils. Also included, but not shown, is the Cs cell and metal enclosure. The generated magnetic field is not resonant with the external structure and does not radiate—the atoms are in the near field of the generating loops.

## SYSTEM INTEGRATION AND PERFORMANCE

The end-state RF-interrogated physics package was designed with component integration, as shown in Figure 12. Considerations included use of nonmagnetic materials and vacuum packaging to both minimize power consumption by minimizing convective thermal losses and allow for thermal isolation

between the 120°C cesium cell and the 70°C VCSEL operating temperature. The use of independent VCSEL and cell thermal control also results in a high VCSEL yield with a large tolerance in nominal VCSEL emission.

The physics package was assembled as a stack-up on the nonmagnetic vacuum-package header. The VCSEL flex-circuit was followed by integrated cesium-cell, ¼-waveplate, dual-side heater assembly and completed with bonding of a topside photodiode. Wirebonding to the gold-plated pins was performed during the layered assembly.

The z-axis bias field, in the direction of the laser propagation, was designed as a Helmholtz coil arrangement. Due to the use of the end-state transition, bias field nonuniformity leads to hyperfine resonance signal line broadening; hence, field uniformity was designed to better than 0.5% by use of a 15-millimete-diameter Helmholtz coil pair.

With a bias field of about 80 mG, the Zeeman splitting frequency is ~30 kHz. Zeeman state interrogation, needed for dual transition locking to stabilize the system against magnetic field perturbations, was achieved by use of a second coil pair winding, fabricated in the orthogonal direction to the bias-field Helmholtz coil. Both the bias-field and the Zeeman interrogation coils where wound around grooves etched in the outer layer of the metallic vacuum package, minimizing total volume. The x-axis Zeeman interrogation coils followed the contour of the cylindrical vacuum package with dimensions of 8 mm x 11 mm.

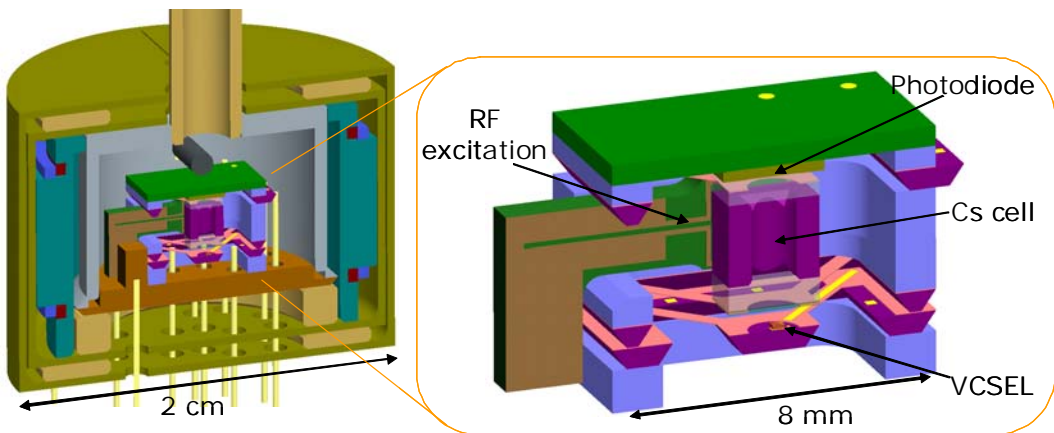


Figure 12. Section view of the physics package showing the inner vacuum package and components (right) and the outer z-axis coils and magnetic shielding layers (left). The tube out the top is for vacuum pinch-off.

A cutaway photo of a fully integrated physics package is shown in Figure 13. This physics package consumed 25 mW when operated with a cesium cell at 120°C and VCSEL-wavelength locked at 70°C, with about 2 mW attributed to VCSEL DC bias. The clock Allan deviation was measured with laboratory electronics. All of the feedback loops were operating: the LO locked to the hyperfine resonance, the Zeeman magnetic field stabilized, the VCSEL wavelength locked to the absorption peak, and the cell temperature under PI control. The deviation follows  $6 \times 10^{-11}/\sqrt{\tau}$  or about  $1 \times 10^{-11}$  at 100 seconds. The system was measured to have a magnetic field sensitivity reduced from a natural end-state value of 2450 kHz/G without Zeeman field lock to a value of 10 Hz/G with the implementation of the dual feedback loops.

The drift seen after an integration time of 200 seconds was investigated. To determine if such a drift was caused by magnetic effects influencing the end-state system, the physics package was run on the 0-0 field insensitive transition. Although not the correct field geometry, a small-contrast resonance signal was still observed and locked. The Allan deviation is shown to have a degraded short-term stability, but follows a  $1/\sqrt{\tau}$  dependence. This 0-0 Allan deviation measurement showed a drift mechanism that follows the same dependence as that seen on the end-state system. This, in addition to measurements of the lab electronics used, indicates that the drift is caused by a temperature effect in the lab-scale control electronics.

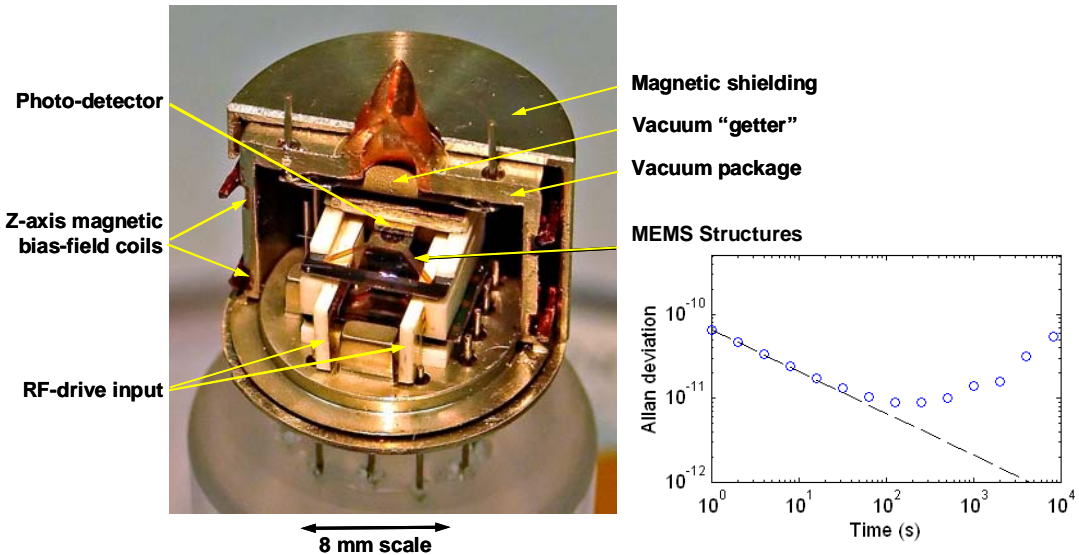


Figure 13. Prototype physics package and performance. Left) Cut-away view of a completed physics package assembly. Right) Allan deviation measured for the prototype. The dashed line is at a value of  $6 \times 10^{-11}/\sqrt{\tau}$ .

Initial compact control electronics were designed and fabricated. Servo control loops were implemented in software, with the electronics controlled by a low-power DSP. Commercial components were utilized for DSP, DACs, and 4.6 GHz VCO electronics. A custom-designed onboard diode-double was used to generate the 9.2 GHz LO signal, with an onboard Wilkenson splitter used to drive the two RF loops on either side of the vapor cell. Figure 14 shows a photo of the initial electronics.



Figure 14. Initial integrated control electronics implemented with DSP servo control and an onboard RF diode-doubler/splitter.

Finally, a physics package was fabricated with a 2 mm pathlength 2.5 atm buffer-gas vapor cell. In this case, the optical absorption lines were completely unresolved, yet still exhibit a strong end-state resonance signal (Figure 15). Note that the optical absorption lines are totally unresolved with this buffer-gas pressure. Such high-pressure cells will be needed for implementing low-power CSACs with submillimeter vapor cells, not achievable when implemented on the 0-0 transition. Hence, a submillimeter vapor cell with high buffer-gas pressure can be implemented with end-state interrogation, enabling aggressive CSAC miniaturization, with natural mechanical vibration resonances in the 10 kHz regime.

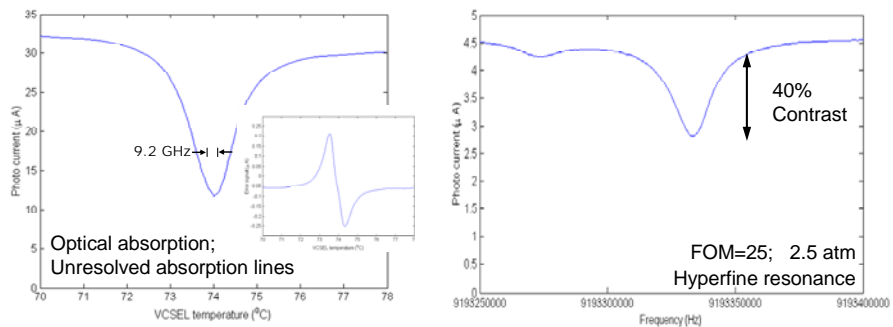


Figure 15. Measurements from a high buffer-gas pressure end-state CSAC. The optical absorption lines are completely unresolved, yet the system still measures a strong resonance signal.

## SUMMARY

An end-state chip-scale atomic clock was designed, fabricated, and characterized. Batch-fabrication techniques were implemented to develop a VCSEL pump laser, alkali-vapor cells, thermally isolating

support structures, temperature sensing and heating elements, and RF-feed loops. A system was designed for a cw VCSEL pump with direct RF hyperfine interrogation. Implementation with a novel dual feedback locking approach onto the end-state hyperfine and Zeeman states allows active control of the local magnetic field for stabilization of the field-sensitive transition against magnetic field perturbations. Strong end-state resonant signal strengths were measured, including greater than 50% contrast signals from 2 mm, 0.7 atm temperature-invariant buffer-gas cells. Such signals were used to produce a 25 mW power-consumption, 4 cm<sup>3</sup> volume physics package with an Allan deviation of  $6 \times 10^{-11}/\sqrt{\tau}$ . In addition, 40% contrast end-resonance signals were measured from a 2 mm, 2.5 atm vapor cell CSAC, all in the regime of optically unresolved lines. Such a measurement portends the use of submillimeter high-pressure vapor cells for aggressively miniaturized CSAC with low power consumption and mechanical resonances in the 10 kHz regime for high shock and vibration environments.

## ACKNOWLEDGMENTS

The authors thank Dr. Aly Fathy and Alex Zhang, University of Tennessee at Knoxville, for initial design of the RF structure, David New for design of magnetic shielding, and Fran McGinty for design of the onboard diode-doubler and Wilkenson splitter.

The research reported in this document/presentation was performed by Sarnoff in connection with contract/instrument NBCHC020045 with the Department of the Interior. The views and conclusions contained in this document/presentation are those of the authors and should not be interpreted as presenting the official policies or position, either expressed or implied, of the Department of the Interior or the U.S. Government unless so designated by other authorized documents. Citation of manufacturer's or trade names does not constitute an official endorsement or approval of the use thereof. The U.S. Government is authorized to reproduce and distribute reprints for government purposes, notwithstanding any copyright notation herein.

**Distribution Statement A.** Approved for public release; distribution is unlimited.

## REFERENCES

- [1] J. Kitching, L. Hollberg, S. Knappe, and R. Wynands, 2001, “*Compact atomic clock based on coherent population trapping,*” **Electronics Letters** **37**, (24), 1449-1451.
- [2] R. Lutwak, P. Vlitas, M. Varghese, M. Mescher, D. K. Serkland, and G. M. Peake, 2005, “*The MAC –a Miniature Atomic Clock,*” in Proceedings of the 2005 Joint IEEE International Frequency Control Symposium and Precise Time & Time Interval (PTTI) Systems & Applications Meeting, 29-31 August 2005, Vancouver, Canada (IEEE Publication 05CH37664C), pp. 752-757.
- [3] M. Zhu, L. S. Cutler, J. E. Berberian, J. F. DeNatale, P. A. Stupar, and C. Tsai, 2004, “*Narrow Linewidth CPT Signal in Small Vapor Cells for Chip Scale Atomic Clocks,*” in Proceedings of the 2004 IEEE International Ultrasonics, Ferroelectrics, and Frequency Control Joint 50<sup>th</sup> Anniversary Conference, 23-27 August 2004, Montreal, Canada (IEEE Publication), pp. 100-103.
- [4] D. W. Youngner, L. M. Lust, D. R. Carlson, S. T. Lu, L. J. Forner, H. M. Chanhvongsak, and T. D. Stark, 2007, “*A Manufacturable Chip-Scale Atomic Clock,*” in Proceedings of the 14<sup>th</sup> International Conference on Solid-State Sensors, Actuators, and Microsystems, 10-14 June 2007, Lyon, France (IEEE Publication TH8933), pp. 39-44.

- [5] D. K. Walter and W. Happer, 2002, “*Spin-exchange broadening of atomic clock resonances*,” **Laser Physics**, **12**, 1182-1187.
- [6] A. B. Post, Y.-Y. Jau, N. N. Kuzma, A. M. Braun, S. Lipp, J. H. Abeles, M. Romalis, E. Miron, and W. Happer, 2002, “*End-Resonance for Atomic Clocks*,” in Proceedings of the 34<sup>th</sup> Annual Precise Time and Time Interval (PTT) Systems and Applications Meeting, 3-5 December 2002, Reston, Virginia, USA (U.S. Naval Observatory, Washington, D.C.), pp. 445-456.
- [7] Y.-Y. Jau, A. B. Post, N. N. Kuzma, A. M. Braun, M. V. Romalis, and W. Happer, 2004, “*Intense, narrow atomic-clock resonances*,” **Physical Review Letters**, **92**, 110801-1 – 110801-4.
- [8] M. H. Kwakernaak, S. Lipp, S. McBride, P. Zanzucchi, W. K. Chan, V. B. Khalfin, H. An, R. D. Whaley Jr., B. I. Willner, A. Ulmer, J. Z. Li, T. J. Davis, A. M. Braun, J. H. Abeles, A. Post, Y.-Y. Jau, N. N. Kuzma, and W. Happer, 2004, “*Components for batch fabricated chip-scale atomic clocks*,” in Proceedings of the 36<sup>th</sup> Annual Precise Time and Time Interval (PTTI) Systems and Applications Meeting, 7-9 December 2004, Washington, D.C., USA (U.S. Naval Observatory, Washington, D.C.), pp. 355-367.
- [9] R. Lutwak, D. Emmons, T. English, W. Riley, A. Duwel, M. Varghese, D. K. Serland, and G. M. Peake, 2003, “*Chip-Scale Atomic Clock, Recent Development Progress*,” in Proceedings of the 35<sup>th</sup> Annual Precise Time and Time Interval (PTTI) Systems and Applications Meeting, 2-4 December 2003, San Diego, California, USA (U.S. Naval Observatory, Washington, D.C.), pp. 467-478.

*39<sup>th</sup> Annual Precise Time and Time Interval (PTTI) Meeting*